Ultra-Low-Power Cryogenic SiGe Low-Noise Amplifiers: Theory and Demonstration

Shirin Montazeri, *Student Member, IEEE*, Wei-Ting Wong, *Student Member, IEEE*, Ahmet H. Coskun, *Student Member, IEEE*, and Joseph C. Bardin, *Member, IEEE*

***Abstract*—Low-power cryogenic low-noise amplifiers (LNAs) are desired to ease the cooling requirements of ultra-sensitive cryogenically cooled instrumentation. In this paper, the tradeoff between power and noise performance in silicon–germanium LNAs is explored to study the possibility of operating these devices from low supply voltages. A new small-signal heterojunction bipolar transistor noise model applicable to both the forward-active and saturation regimes is developed from first principles. Experimental measurements of a device across a wide range of temperatures are then presented and the dependence of the noise parameters on collector–emitter voltage is described. This paper concludes with the demonstration of a high-gain 1.8–3.6-GHz cryogenic LNA achieving a noise temperature of 3.4–5 K while consuming just 290 μW when operating at 15-K physical temperature.**

***Index Terms*—Cryogenic low-noise amplifier (LNA), low power, radio astronomy, silicon–germanium (SiGe) heterojunction bipolar transistor (HBT).**

I. Introduction

CRYOGENICALLY cooled microwave low-noise amplifiers (LNAs) are a critical component in a number of important applications requiring very high sensitivity receivers. State-of-the-art cryogenic LNAs employ InP high-electron mobility transistors (HEMTs) or silicon–germanium (SiGe) heterojunction bipolar transistors (HBTs) and, when cooled to 15-K physical temperature, regularly achieve sub-5-K noise temperatures over the 1–10-GHz frequency range (e.g., [1]–[4]). While this level of performance has been sufficient to enable the success of many high-impact instruments, limited research has focused on determining and achieving the fundamental limits for the power consumption of these amplifiers. Consequentially, typical cryogenic LNAs require at least 4 mW of dc power to operate with nominal performance [2]–[8].

The maximum power that can be consumed by cryogenic electronics is ultimately limited by the heat removal capabilities of the cooling system, which, for typical closed-cycle coolers, ranges from hundreds of microwatts at a physical temperature of 100 mK [9] to 1.5 W at 4.2-K physical temperature [10] and 12 W at 20-K physical temperature [11]. Today, there are a number of emerging applications in which the power dissipation of currently available cryogenic LNAs places serious constraints on system design. These applications include terahertz heterodyne cameras, where IF amplifiers are required for large arrays of superconductor–insulator–superconductor (SIS) [12]–[14] or hot-electron bolometer (HEB) [15] mixers, microwave quantum computing, in which large numbers of (potentially multiplexed) qubits must be read out [16], [17], balloon-based instruments, in which the evaporation rate of precious liquid cryogens is directly proportional to the power dissipation of the cryogenic electronics [18], and various experiments in fundamental physics, in which cryogenic amplifiers must be closely interfaced with devices at milli-kelvin temperatures [19], [20]. For each of these fields, the development of amplifiers with greatly reduced power consumption would enable significant advances in the associated instrumentation.

The noise and small-signal properties of an HBT are a strong function of the quiescent collector current density ($J_{\rm C}$), and the realization of optimum system noise performance requires biasing a device near the current density associated with the global minima of its cascaded noise temperature, $T_{\rm CAS} = T_0 M = T_{\rm e}/(1 - 1/G_{\rm AV})$ [4], [21], [22], where $T_0 = 290$ K is the reference temperature, M is the noise measure, $T_{\rm e}$ is the noise temperature, and $G_{\rm AV}$ is the available gain. Moreover, in broadband applications, the device periphery is typically constrained to a relatively narrow range of values for which the optimum generator resistance is close to 50 Ω. Therefore, in trying to minimize the power consumption of HBT-based cryogenic LNAs, it is important to determine the minimum collector–emitter voltage that can be used.

The idea of employing a weakly saturated[1] SiGe HBT to achieve ultra-low-power amplification was proposed based on experimental observations in [23] and an X-band room-temperature LNA running from a 0.5-V supply and consuming 2.5 mW was later reported [24]. However, to the best of the authors' knowledge, no detailed study of the noise performance of SiGe HBTs at low-$V_{\rm CE}$ has previously been carried out, nor have the theoretical performance limitations for low $V_{\rm CE}$ operation been reported. In this paper, the tradeoff between noise performance and collector–emitter voltage is examined over a wide range of

Manuscript received June 03, 2015; revised September 25, 2015; accepted October 26, 2015. Date of publication November 13, 2015; date of current version January 01, 2016. This work was supported by the National Science Foundation (NSF) under CAREER Grant CCCS-1351744 and by the Office of Naval Research (ONR) under Grant N00014-12-1-0991.

The authors are with the Department of Electrical and Computer Engineering, University of Massachusetts at Amherst, Amherst, MA 01003-9292 USA (e-mail: jbardin@engin.umass.edu).

Color versions of one or more of the figures in this paper are available online at http://ieeexplore.ieee.org.

Digital Object Identifier 10.1109/TMTT.2015.2497685

[1]The weakly saturated regime describes the range of collector–emitter voltages between approximately 0.5 V and the onset of strong saturation.

temperatures and, leveraging the resulting theoretical and experimental conclusions, a high-gain octave-bandwidth cryogenic LNA consuming less than 300 μW is demonstrated. This paper is organized as follows.

1) The theoretical implications of operating at low-V_{CE} are discussed and, based on first principles, a small-signal noise model is developed.
2) The small- and large-signal terminal characteristics of an example device are presented as a function of collector–emitter voltage and the expected impact on noise performance is discussed.
3) The small-signal noise model of an example device is extracted and the noise parameters are studied as a function of collector–emitter voltage.
4) A discrete transistor cryogenic LNA is presented and the measured performance is compared to simulation and other published cryogenic amplifier results.

II. Theoretical Noise Performance of HBTs at Low V_{CE}

Reducing V_{CE} has three important consequences on device performance. First, the base–collector junction capacitance will increase with the narrowing of the base–collector depletion region. This change must be quantified and incorporated into designs, but is not expected to be detrimental to performance at frequencies below $f_{\max}/10$, where $f_{\max}$ is the maximum frequency of oscillation of the transistor. Secondly, as the device enters the weakly saturated regime, base–collector diffusion current will result in a further increase in C_{CB}. As the transistor enters strong saturation, this capacitance will dominate C_{CB} and will ultimately limit the RF performance of the device.

The final consequence of operating at low V_{CE} is the generation of additional shot-noise due to the diffusion of carriers across the collector–base junction. The impact of this excess shot noise can be quantified by studying the expressions for the total base and collector currents

$$I_{\mathrm{B}} = I_{\mathrm{BF}} + I_{\mathrm{BR}} \tag{1}$$

and

$$I_{\mathrm{C}} = I_{\mathrm{CF}} - I_{\mathrm{CR}} - I_{\mathrm{BR}} \tag{2}$$

where I_{BF} and I_{BR} are the base current components flowing from the base to the emitter and from the base to the collector, respectively, and I_{CF} and I_{CR} are the forward and reverse collector current components, respectively. Expressions for the base and collector shot noise components in the weakly saturated regime can be readily written from (1) and (2),

$$\overline{|i_{\mathrm{n,b}}|^2} = 2q\left(I_{\mathrm{BF}} + I_{\mathrm{BR}}\right)\Delta f = 2qI_{\mathrm{B}}\Delta f \tag{3}$$

$$\begin{aligned}\overline{|i_{\mathrm{n,c}}|^2} &= 2q\left(I_{\mathrm{CF}} + I_{\mathrm{CR}} + I_{\mathrm{BR}}\right)\Delta f \\ &= 2qI_{\mathrm{CF}}\left(2 - \frac{I_{\mathrm{C}}}{I_{\mathrm{CF}}}\right)\Delta f\end{aligned} \tag{4}$$

and

$$\overline{i_{\mathrm{n,b}} i_{\mathrm{n,c}}^{*}} = -2qI_{\mathrm{BR}}\Delta f. \tag{5}$$

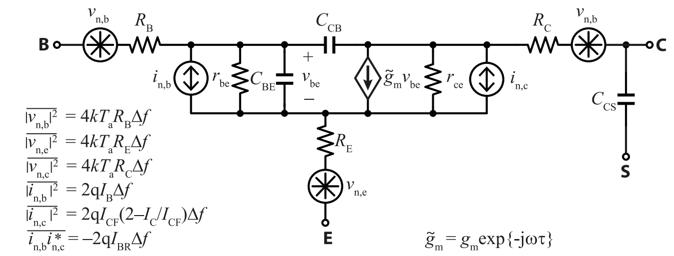

Fig. 1. General HBT small-signal noise model. In the forward-active mode of operation, $I_{\mathrm{C}} = I_{\mathrm{CF}}$ and $I_{\mathrm{B}} = I_{\mathrm{BF}}$ and the model simplifies to the standard HBT noise model.

These expressions are valid in both the forward-active and saturation regimes and at frequencies well below f_{t}, where standard shot-noise correlation effects between the forward-active mode currents are small and can be neglected [25], [26].

A small-signal noise model for a SiGe HBT on a semiconducting substrate is shown in Fig. 1. The model can be used to describe the performance of modern SiGe HBTs in both the forward-active and saturation regimes and to frequencies in the 40-GHz region. While this frequency range is sufficient for the design of broadband microwave amplifiers, a higher order model, including base–collector capacitance splitting and forward-active mode shot noise correlation is required at millimeter-wave frequencies [27].

Approximate expressions for the noise parameters and associated gain have been derived in the high dc current gain limit and for $R_{\mathrm{B}} \gg R_{\mathrm{E}}$ and $g_{\mathrm{m}} \gg \omega C_{\mathrm{CB}}$. The resulting expressions (6)–(10), shown at the bottom of the following page, are in terms of the forward-active transconductance (g_{mF}), ideality factor $(n_{\mathrm{cF}} = qI_{\mathrm{CF}}/g_{\mathrm{mF}}kT_{\mathrm{a}})$, and dc current gain $(\beta_{\mathrm{F}} = I_{\mathrm{CF}}/I_{\mathrm{BF}})$ so that the only parameters that depend upon V_{CE} are the unity-current gain cutoff frequency (f_{t}), I_{C}, I_{B}, C_{CB}, and R_{B}. Of these parameters, R_{B} is expected to only display a weak dependence on V_{CE}. In the limiting case of $I_{\mathrm{C}} = I_{\mathrm{CF}}$ and $I_{\mathrm{B}} = I_{\mathrm{BF}}$, these expressions simplify to the equations corresponding to the forward-active mode of operation.

Inspection of equations (6)–(10) reveals several mechanisms through which the noise performance may degrade at low collector–emitter voltages.

- The low-frequency value of T_{MIN} is strongly dependent upon the dc current gain, $\beta = I_{\mathrm{C}}/I_{\mathrm{B}}$. As the device enters the saturation regime, β is expected to rapidly decrease, thereby resulting in a sharp degradation to the noise performance.
- The high-frequency value of T_{MIN} is proportional to $(f/f_{\mathrm{t}})\sqrt{R_{\mathrm{B}}\left(2 - I_{\mathrm{C}}/I_{\mathrm{CF}}\right)}$. While R_{B} is not expected to display a significant dependence on V_{CE}, f_{t} is expected to drop significantly as the device enters the weakly saturated regime. Therefore, a rapid rise in the high-frequency limit of T_{MIN} is anticipated for values of V_{CE} for which a significant decline in f_{t} is observed.
- The optimum generator impedance will tend toward a short circuit as the device enters the deep-saturation regime due to a sharp rise in base current and the associated shot noise.
- The noise resistance, R_{N}, is expected to be independent of V_{CE} until saturation currents begin to flow, at which point R_{N} will rapidly rise as I_{C} tends to zero.

- The associated gain is proportional to f_{t} and inversely proportional to C_{CB}. Therefore, as the device enters the weak saturation regime, an increase in C_{CB} and the related drop in f_{t} will result in a significant drop in G_{ASSOC}.

From the discussion above, it is evident that the terminal characteristics of a SiGe HBT can be studied to gain insight into the dependence of the noise performance on the applied collector–emitter voltage. In the following section, the dc, ac, and intermodulation characteristics of a representative HBT are reported.

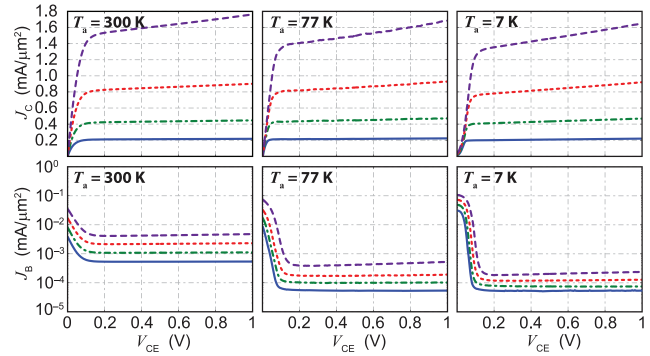

Fig. 2. Collector/base current densities as a function of collector–emitter voltage at 300 K (*left*), 77 K (*center*), and 7 K (*right*).

III. Terminal Characteristics at Low-V_{CE}

An $18 \times 0.12\ \mu\mathrm{m}^2$ IBM BiCMOS8HP[2] transistor was characterized at 7, 77, and 300 K using a cryogenic wafer probe station. Measurements of the dc characteristics were carried out with the transistor terminated at RF to prevent oscillation. Scattering parameters were measured from 0.01 to 67 GHz using an Agilent N-5247A vector network analyzer. Parasitic effects related to the bondpads and feed-lines were removed using a pad/open/short de-embedding algorithm [28]. From previous studies, it is known that the nominal bias point for low-noise SiGe microwave amplifiers lies in the range of 0.1–2 $\mathrm{mA}/\mu\mathrm{m}^2$ [4]. Therefore, the range of current densities presented here was selected within this range.

A. DC Characteristics

The base and collector current densities of the device were measured as a function of V_{CE} for fixed V_{BE}. Example measurement results appear in Fig. 2. These bias points cover an order of magnitude of current densities ranging from low- to medium-injection. The collector current demonstrated a transition from saturation to the forward-active region for collector voltages in the 50–100-mV range. Slight to moderate slopes were observed in the forward-active region at all temperatures, indicating a dependence of J_{CF} on V_{CE} through the Early effect [29], [30]. While this is expected to have only a small effect for current densities below 0.5 $\mathrm{mA}/\mu\mathrm{m}^2$, the dependence of J_{CF} on V_{CE} should be considered when modeling the noise performance using (4). For subsequent discussion, the variable J_{CF0} is used to represent the value of the forward collector–current density at $V_{\mathrm{CB}} = 0$ V.

At each temperature, the base current exhibited a clear transition from forward-active mode operation to saturation as the base–collector junction became forward biased. The onset of reverse base current occurred for base–collector voltages in the range of 100–150 mV below the applied base–emitter voltages, which is explained by the high Ge content at the collector edge of the base and the comparatively lighter doping of the intrinsic collector, both of which contribute to a lower built-in potential across the base–collector space-charge region (SCR) in comparison to that of the base–emitter SCR. An interesting feature is that the sharpness of the base–collector junction turn-on

[2]While this technology was chosen due to its maturity, measurements of devices from other advanced technology platforms (e.g., TowerJazz SBC18H3 and ST BiCMOS9MW) indicate that the general results apply to other aggressively scaled SiGe HBTs.

$$T_{\mathrm{MIN}} \approx n_{\mathrm{cF}} T_{\mathrm{a}} \left[g_{\mathrm{mF}} R_{\mathrm{B}} \left(2 - \frac{I_{\mathrm{C}}}{I_{\mathrm{CF}}}\right) \left(\frac{f}{f_{\mathrm{t}}}\right)^2 + \sqrt{\frac{1}{\beta_{\mathrm{F}}} \frac{I_{\mathrm{B}}}{I_{\mathrm{BF}}} \left[\frac{I_{\mathrm{CF}}}{I_{\mathrm{C}}} \left(2 \frac{I_{\mathrm{CF}}}{I_{\mathrm{C}}} - 1\right) + \frac{2 g_{\mathrm{mF}} R_{\mathrm{B}}}{n_{\mathrm{cF}}} \right] + \frac{2 g_{\mathrm{mF}} R_{\mathrm{B}}}{n_{\mathrm{cF}}} \left(2 - \frac{I_{\mathrm{C}}}{I_{\mathrm{CF}}}\right) \left(\frac{f}{f_{\mathrm{t}}}\right)^2} \right] \tag{6}$$

$$R_{\mathrm{OPT}} \approx \frac{\beta_{\mathrm{F}}}{g_{\mathrm{mF}}} \frac{\sqrt{\left(\frac{1}{\beta_{\mathrm{F}}}\right) \left(\frac{I_{\mathrm{B}}}{I_{\mathrm{BF}}}\right) \left[\left(\frac{I_{\mathrm{CF}}}{I_{\mathrm{C}}}\right) \left(2 \left(\frac{I_{\mathrm{CF}}}{I_{\mathrm{C}}}\right) - 1\right) + \left(\frac{2 g_{\mathrm{mF}} R_{\mathrm{B}}}{n_{\mathrm{cF}}}\right) \right] + \left(\frac{2 g_{\mathrm{mF}} R_{\mathrm{B}}}{n_{\mathrm{cF}}}\right) \left(2 - \left(\frac{I_{\mathrm{C}}}{I_{\mathrm{CF}}}\right)\right) \left(\frac{f}{f_{\mathrm{t}}}\right)^2}}{\frac{I_{\mathrm{B}}}{I_{\mathrm{BF}}} + \beta_{\mathrm{F}} \left(2 - \frac{I_{\mathrm{C}}}{I_{\mathrm{CF}}}\right) \left(\frac{f}{f_{\mathrm{t}}}\right)^2} \tag{7}$$

$$X_{\mathrm{OPT}} \approx \frac{\beta_{\mathrm{F}}}{g_{\mathrm{mF}}} \frac{I_{\mathrm{CF}}}{I_{\mathrm{C}}} \frac{f}{f_{\mathrm{t}}} \frac{2 - I_{\mathrm{C}}/I_{\mathrm{CF}}}{(I_{\mathrm{B}}/I_{\mathrm{BF}}) + \beta_{\mathrm{F}} (2 - I_{\mathrm{C}}/I_{\mathrm{CF}}) (f/f_{\mathrm{t}})^2} \tag{8}$$

$$R_{\mathrm{N}} \approx \frac{T_{\mathrm{a}}}{T_0} \left(R_{\mathrm{B}} + \frac{n_{\mathrm{cF}}}{2 g_{\mathrm{mF}}} \frac{I_{\mathrm{CF}}}{I_{\mathrm{C}}} \left(2 \frac{I_{\mathrm{CF}}}{I_{\mathrm{C}}} - 1\right) \right) \tag{9}$$

$$G_{\mathrm{ASSOC}} \approx \frac{f_{\mathrm{t}}}{f} \frac{n_{\mathrm{cF}}/2}{2\pi f C_{\mathrm{CB}} R_{\mathrm{B}}} \sqrt{\frac{1}{\beta_{\mathrm{F}}} \frac{I_{\mathrm{B}}}{I_{\mathrm{BF}}} \left(\frac{I_{\mathrm{CF}}}{I_{\mathrm{C}}} \left(2 \frac{I_{\mathrm{CF}}}{I_{\mathrm{C}}} - 1\right) + 2 \frac{g_{\mathrm{mF}} R_{\mathrm{B}}}{n_{\mathrm{cF}}} \right) + 2 \frac{g_{\mathrm{mF}} R_{\mathrm{B}}}{n_{\mathrm{cF}}} \left(2 - \frac{I_{\mathrm{C}}}{I_{\mathrm{CF}}}\right) \left(\frac{f}{f_{\mathrm{t}}}\right)^2} \tag{10}$$

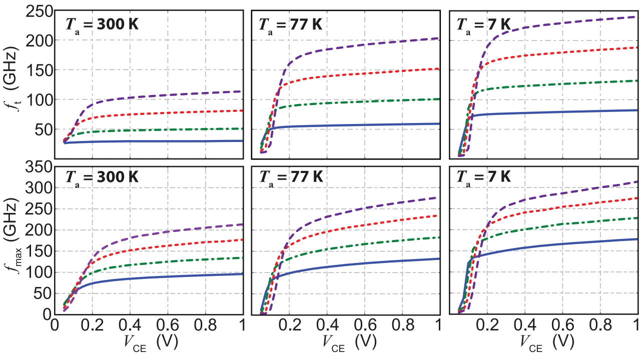

Fig. 3. Unity current gain cutoff frequency/maximum frequency of oscillation versus collector–emitter voltage at 300 K (*left*), 77 K (*center*), 7 K (*right*). Data are plotted for J_{CF0} equal to 0.22 mA/μm^2 (solid blue line), 0.46 mA/μm^2 (green dashed–dotted line), 0.92 mA/μm^2 (red dotted line), and 1.67 mA/μm^2 (purple dashed line).

demonstrated a strong temperature dependence, with significantly larger deep-saturation base currents flowing at cryogenic temperatures.

B. AC Terminal Characteristics

The de-embedded scattering parameters of the 18×0.12 μm^2 SiGe HBT were obtained over a wide range of biases and used to find the unity current gain cutoff frequency and the maximum frequency of oscillation as a function of V_{CE}. The base–emitter voltage was held constant during the sweeps. Example results are shown in Fig. 3. The bias points for these data correspond to those shown in Fig. 2. For a fixed value of J_{CF0}, a significant enhancement of f_{t} was observed with cryogenic cooling. This result is consistent with previously reported results [4], [31]–[33] and is explained by an improved transconductance at cryogenic temperatures. In the forward-active mode of operation, the f_{t} curves exhibit a positive slope, which can be explained by the dependence of C_{CB} on V_{CB}. In comparison to the dc terminal characteristics, the knee voltages for the f_{t} curves demonstrate a significantly stronger dependence on collector current density. This relationship is explained by the increased base voltage required to support a larger current density, resulting in a proportionally larger base–collector voltage.

A significant increase in the maximum frequency of oscillation was also observed with cryogenic cooling (Fig. 3). Again, a slope was observed in the forward-active region of the curves due to an increase in C_{CB} as the base–collector voltage increased. The observed knee voltage was found to be weakly dependent on temperature and, as expected, was proportional to J_{CF0}.

C. Nonlinearity

The impact of low-V_{CE} operation on dynamic range is an important consideration for devices used in practical LNAs, which often must operate over a wide range of input signal amplitudes. The 50-Ω output-referred third-order intermodulation intercept (OIP_3) of the 18×0.12 μm^2 SiGe HBT was measured as a function of current density and collector–emitter voltage at 7, 77, and 300 K and example results appear in Fig. 4. At low-current densities, the nonlinearity was only weakly dependent upon the

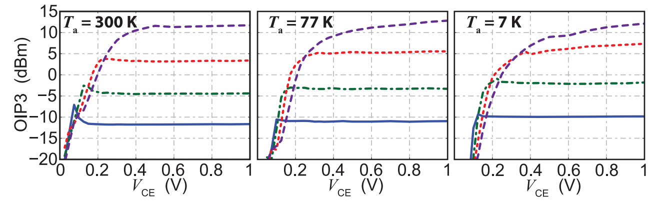

Fig. 4. Output-referred third-order inter-modulation intercept at 300 K (*left*), 77 K (*center*), and 7 K (*right*). Measurement data are taken at 3 GHz and referenced to the bondpads of the test structure. The general behavior is only weakly frequency dependent. Data are plotted for J_{CF0} equal to 0.22 mA/μm^2 (solid blue line), 0.46 mA/μm^2 (green dashed–dotted line), 0.92 mA/μm^2 (red dotted line), and 1.67 mA/μm^2 (purple dashed line).

collector–emitter voltage, provided the device was in the forward-active region. However, when the device was biased towards the medium-injection region, corresponding to collector current densities above 1 mA/μm^2, a significant degradation to linearity was observed for collector–emitter voltages as high as 400 mV.

D. Discussion

Based upon the results presented in Sections III-A–III-C, the following general conclusions can be made.

- From an aggregate analysis of dependence of the terminal characteristics on the collector–emitter voltage, it appears feasible to operate SiGe HBTs in the low-injection region with collector–emitter voltages on the order of 100–200 mV without degradation to any of the terminal characteristics.
- In general, as the current density is increased towards the medium-injection regime, a larger collector–emitter voltage is required to maintain nominal performance.
- Even in the medium-injection regime, it appears to be possible to operate with collector–emitter voltages on the order of 200 mV if linearity is not critical.

IV. Dependence of Noise Performance on V_{CE}

For an HBT to be used in a robust LNA, its noise parameters should be insensitive to the applied collector–emitter voltage. Therefore, the minimum permissible value of V_{CE} for a device targeted for a low-noise application is ultimately determined by the range of voltages for which the noise parameters and associated gain are stable. Conceptually, this range corresponds to that within which the variables appearing in (6)–(10) are insensitive to V_{CE}. From the results presented in Section III, it is clear that this range is dependent upon current density and extends as low as 100 mV for bias points corresponding to the low-injection regime.

To validate this intuition, the full noise model (see Fig. 1) was extracted as a function of both collector current density and collector–emitter voltage. These experimentally based models were then used to study the noise parameters and associated gain.

A. Noise Model Extraction and Verification

The small-signal model parameters were extracted across a wide range of current densities and collector–emitter voltages using standard parameter extraction techniques. Specifically, the emitter and collector resistances were determined

TABLE I
EXTRACTED MODEL PARAMETERS AT SELECTED BIAS POINTS

$T_a = 7$ K					$R_E = 1.7$			$R_C = 6.7$				
V_{CE}	J_{CF}	J_C	J_{BF}	J_B	R_B	r_{be}	r_{ce}	g_m	C_{BE}	C_{CB}	C_{CS}	τ
1.00	0.22	0.22	3.9e-5	3.9e-5	10.6	227k	43k	34	51	13	2	0.8
0.20	0.20	0.20	3.9e-5	4.1e-5	10.2	222k	43k	31	51	14	2	0.9
0.15	0.20	0.20	3.9e-5	4.4e-5	10.4	210k	43k	31	51	14	2	0.9
0.10	0.20	0.20	3.9e-5	5.0e-5	11.4	151k	43k	31	56	16	2	1.1
1.00	0.47	0.47	7.2e-5	7.2e-5	12.5	121k	14k	65	60	13	2	1.0
0.20	0.41	0.41	7.2e-5	7.2e-5	12.3	136k	14k	59	60	15	2	1.0
0.15	0.41	0.41	7.2e-5	7.3e-5	12.5	121k	14k	59	62	15	2	1.1
0.10	0.40	0.40	7.2e-5	9.3e-5	15.4	41k	14k	56	79	21	2	1.5
1.00	0.92	0.92	1.3e-4	1.3e-4	15.3	52k	6k	116	74	13	2	1.1
0.20	0.77	0.77	1.3e-4	1.3e-4	14.7	76k	6k	104	75	15	2	1.3
0.15	0.76	0.76	1.3e-4	1.3e-4	15.8	60k	6k	102	83	17	2	1.4
0.10	0.76	0.75	1.3e-4	3.2e-4	15.6	7k	1k	86	156	53	2	1.8
1.00	1.65	1.65	2.6e-4	2.6e-4	18.1	19k	3k	188	92	13	2	1.2
0.20	1.34	1.34	2.6e-4	2.6e-4	17.7	28k	3k	156	102	17	2	1.5
0.15	1.32	1.32	2.6e-4	2.6e-4	19.0	19k	3k	154	134	24	2	1.8
0.10	1.30	1.24	2.6e-4	2.1e-3	19.4	0.3k	0.3k	116	535	244	2	1.9

$T_a = 77$ K					$R_E = 1.7$			$R_C = 7.3$				
V_{CE}	J_{CF}	J_C	J_{BF}	J_B	R_B	r_{be}	r_{ce}	g_m	C_{BE}	C_{CB}	C_{CS}	τ
1.00	0.22	0.22	4.4e-5	4.4e-5	9.5	205k	82k	21	43	13	5	0.5
0.20	0.20	0.20	4.4e-5	4.6e-5	9.3	201k	82k	20	43	18	6	0.5
0.15	0.20	0.20	4.4e-5	4.6e-5	9.5	186k	82k	20	44	19	7	0.6
0.10	0.20	0.20	4.4e-5	5.6e-5	10.0	153k	82k	20	45	21	7	0.6
1.00	0.46	0.46	8.3e-5	8.3e-5	11.4	106k	22k	42	49	13	5	0.6
0.20	0.43	0.43	8.3e-5	8.3e-5	11.0	116k	22k	40	50	18	6	0.6
0.15	0.42	0.42	8.3e-5	8.8e-5	11.0	112k	22k	40	50	19	7	0.6
0.10	0.42	0.42	8.3e-5	1.0e-4	12.1	66k	22k	39	57	26	7	0.8
1.00	0.98	0.98	1.6e-4	1.6e-4	13.4	52k	7k	77	59	13	5	0.6
0.20	0.78	0.78	1.6e-4	1.6e-4	13.2	67k	7k	70	59	19	6	0.7
0.15	0.77	0.77	1.6e-4	1.6e-4	13.2	63k	7k	70	63	20	7	0.7
0.10	0.76	0.76	1.6e-4	2.5e-4	16.5	15k	2k	65	100	49	7	1.0
1.00	1.65	1.65	3.2e-4	3.2e-4	16.2	22k	3k	130	73	13	5	0.7
0.20	1.37	1.37	3.2e-4	3.2e-4	15.3	37k	3k	115	76	19	6	0.8
0.15	1.35	1.35	3.2e-4	3.2e-4	16.6	26k	3k	110	96	26	7	1.0
0.10	1.33	1.32	3.2e-4	9.3e-4	17.1	3k	0.5k	89	319	208	7	2.0

$T_a = 300$ K					$R_E = 2.6$			$R_C = 10.2$				
V_{CE}	J_{CF}	J_C	J_{BF}	J_B	R_B	r_{be}	r_{ce}	g_m	C_{BE}	C_{CB}	C_{CS}	τ
1.00	0.22	0.22	4.6e-4	4.6e-4	8.6	43k	110k	8	35	13	6	0.5
0.20	0.21	0.21	4.6e-4	4.6e-4	7.3	45k	56k	8	35	19	7	0.5
0.15	0.21	0.21	4.6e-4	4.6e-4	7.3	43k	22k	8	35	21	8	0.5
0.10	0.21	0.21	4.6e-4	5.6e-4	7.0	37k	5k	8	35	25	8	0.5
1.00	0.46	0.46	1.1e-3	1.1e-3	9.7	20k	32k	17	40	13	6	0.5
0.20	0.44	0.44	1.1e-3	1.1e-3	8.4	22k	16k	16	39	19	7	0.5
0.15	0.44	0.44	1.1e-3	1.1e-3	8.2	20k	9k	16	39	22	8	0.5
0.10	0.44	0.42	1.1e-3	1.5e-3	7.8	18k	2k	16	39	30	8	0.6
1.00	0.94	0.94	2.2e-3	2.2e-3	11.2	10k	10k	33	48	14	6	0.5
0.20	0.86	0.86	2.2e-3	2.2e-3	9.5	12k	7k	31	46	21	7	0.6
0.15	0.85	0.85	2.2e-3	2.2e-3	9.3	11k	3k	30	45	25	8	0.6
0.10	0.85	0.81	2.2e-3	2.6e-3	8.7	8k	0.8k	29	45	41	8	0.6
1.00	1.68	1.68	3.5e-3	3.5e-3	13.4	7k	4k	57	58	14	6	0.5
0.20	1.46	1.46	3.5e-3	3.5e-3	11.0	8k	2k	51	54	18	7	0.6
0.15	1.44	1.44	3.5e-3	3.5e-3	10.4	8k	1k	50	54	31	8	0.7
0.10	1.43	1.35	3.5e-3	4.1e-3	9.4	4k	0.2k	46	55	67	8	0.8

Units–Voltage: V, Current: mA/μm^2, Resistance: $\Omega \cdot \mu$m^2, Conductance: mS/μm^2, Capacitance: fF/μm^2, Delay: ps.

using the open-collector method [34], the collector–substrate and base–collector capacitances were found using cold-bias measurements [35], and the remaining parameters were found using active-bias measurements [35], [36]. The complete set of extracted model parameters appear for selected bias points in Table I. In all cases, the bias dependence of the parameters was consistent with expectation.

Example plots comparing the de-embedded 7-K measurements with extracted models appear in Fig. 5. Excellent agreement was observed between the modeled and measured scattering parameters over a wide range of bias conditions. Similar agreement was observed at both 77 and 300 K. For verification of the noise model, the 50-Ω noise figure of the HBT in the saturation regime was measured at room temperature

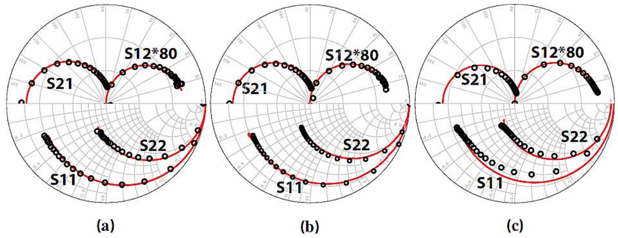

Fig. 5. Comparison of measured and modeled scattering parameters at 7-K physical temperature for $J_{\mathrm{CF0}} = 0.46$ mA/μm^2 at: (a) $V_{\mathrm{CE}} = 500$ mV, (b) $V_{\mathrm{CE}} = 200$ mV, and (c) $V_{\mathrm{CE}} = 100$ mV. Solid lines and markers correspond to the model and measurement, respectively. Data provided from 0.01 to 40 GHz.

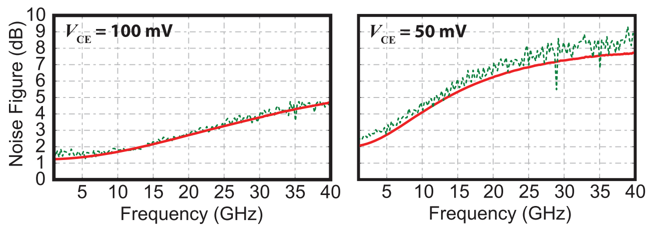

Fig. 6. Room-temperature 50-Ω noise figure referenced to the bondpads of the HBT test structure. For these measurements, $J_{\mathrm{CF0}} = 0.92$mA/μm^2. (*left*) $V_{\mathrm{CE}} = 100$ mV and (*right*) $V_{\mathrm{CE}} = 50$ mV. Solid and dashed lines correspond to the model and measurement, respectively.

using an Agilent N-5247A vector network analyzer with the vector-corrected cold source method [37]. A comparison of the measured and modeled noise figure results, referenced to the test structure bondpads, appears in Fig. 6. Excellent agreement was observed between the predicted and measured 50-Ω noise performance for values of V_{CE} as low as 50 mV.

B. Noise Parameters

Using the complete noise model of Fig. 1, the noise parameters were computed using standard techniques [38] over a wide range of bias and at 7, 77, and 300 K.

1) Minimum Noise Temperature: The minimum noise temperature is plotted as a function of frequency in Fig. 7 and as a function of V_{CE} in Fig. 8. By cooling the transistor from 300 to 7 K, the minimum noise temperature in the forward-active regime improved by a factor of approximately 15. This improvement is consistent with previously reported results [4], [22]. As expected, the minimum noise temperature was nearly independent of V_{CE} until the device became weakly saturated. It is also interesting to note that, in the saturation regime, a much sharper degradation was observed at cryogenic temperatures in comparison to at room temperature. This is related to a significantly sharper collapse in the saturation mode dc current gain and unity current gain cutoff frequency at cryogenic temperatures.

2) Optimum Generator Impedance: The optimum generator resistance and reactance are plotted as a function of V_{CE} in Figs. 9 and 10. As predicted in Section II, both R_{OPT} and X_{OPT} were found to have only weak dependence upon V_{CE} in the forward-active regime and to rapidly decrease in the saturation regime. The saturation-mode behavior was found to be more extreme in the case of cryogenic operation due to the increased base current.

3) Noise Resistance: The degradation in the noise performance of an amplifier that was designed for operation in the

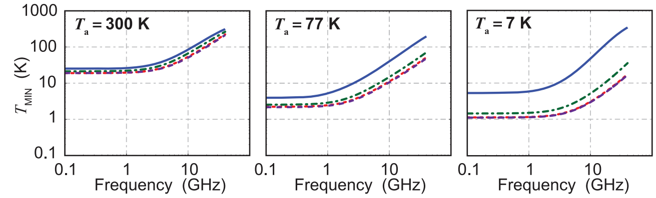

Fig. 7. Minimum noise temperature as a function of frequency at: (*left*) 300-K, (*center*) 77-K, and (*right*) 7-K physical temperature. These data correspond to a bias point of $J_{\mathrm{CF0}} = 0.46$ mA/μm^2. Data are plotted for V_{CE} equal to 75 mV (solid blue line), 100 mV (green dashed–dotted line), 200 mV (red dotted line), and 500 mV (purple dashed line).

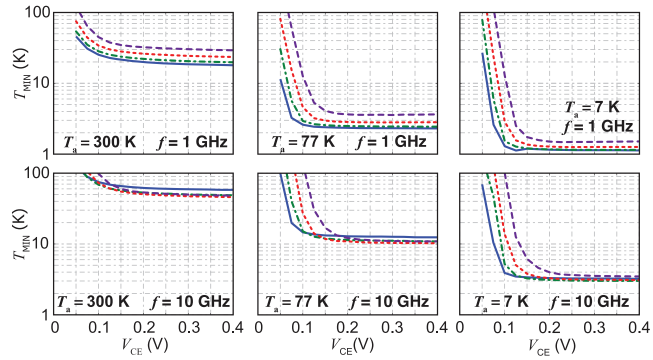

Fig. 8. Minimum noise temperature at 1 and 10 GHz for physical temperatures of: (*left*) 300 K, (*center*) 77 K, and (*right*) 7 K. Data are plotted for J_{CF0} equal to 0.22 mA/μm^2 (solid blue line), 0.46 mA/μm^2 (green dashed–dotted line), 0.92 mA/μm^2 (red dotted line), and 1.67 mA/μm^2 (purple dashed line).

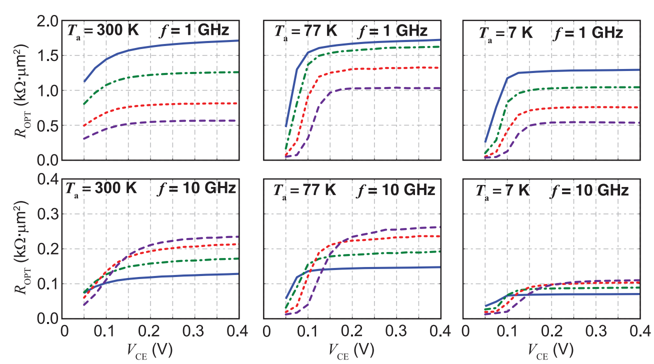

Fig. 9. Optimum generator resistance at 1 and 10 GHz for physical tempeartures of: (*left*) 300 K, (*center*) 77 K, and (*right*) 7 K. Data are plotted for J_{CF0} equal to 0.22 mA/μm^2 (solid blue line), 0.46 mA/μm^2 (green dashed–dotted line), 0.92 mA/μm^2 (red dotted line), and 1.67 mA/μm^2 (purple dashed line).

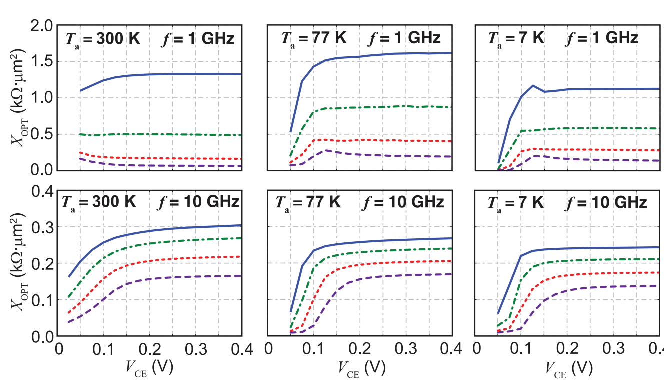

Fig. 10. Optimum generator reactance at 1 and 10 GHz for physical temperatures of: (*left*) 300 K, (*center*) 77 K, and (*right*) 7 K. Data are plotted for J_{CF0} equal to 0.22 mA/μm^2 (solid blue line), 0.46 mA/μm^2 (green dashed–dotted line), 0.92 mA/μm^2 (red dotted line), and 1.67 mA/μm^2 (purple dashed line).

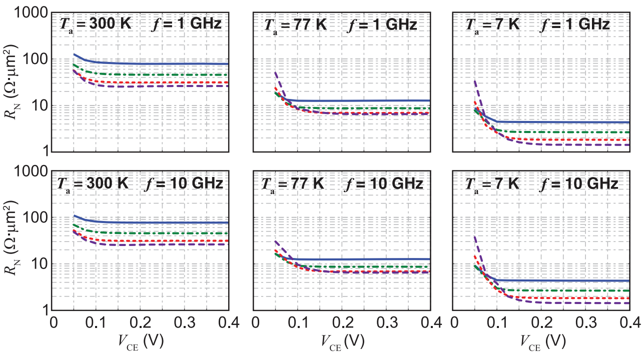

Fig. 11. Noise resistance at 1 and 10 GHz for physical temperatures of: (*left*) 300 K, (*center*) 77 K, and (*right*) 7 K. Data are plotted for J_{CF0} equal to 0.22 mA/μm^2 (solid blue line), 0.46 mA/μm^2 (green dashed–dotted line), 0.92 mA/μm^2 (red dotted line), and 1.67 mA/μm^2 (purple dashed line).

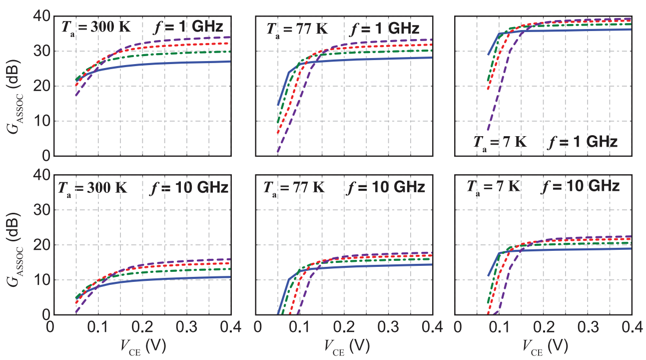

Fig. 12. Associated gain at 1 and 10 GHz for physical temperatures of: (*left*) 300 K, (*center*) 77 K, and (*right*) 7 K. Data are plotted for J_{CF0} equal to 0.22 mA/μm^2 (solid blue line), 0.46 mA/μm^2 (green dashed–dotted line), 0.92 mA/μm^2 (red dotted line), and 1.67 mA/μm^2 (purple dashed line).

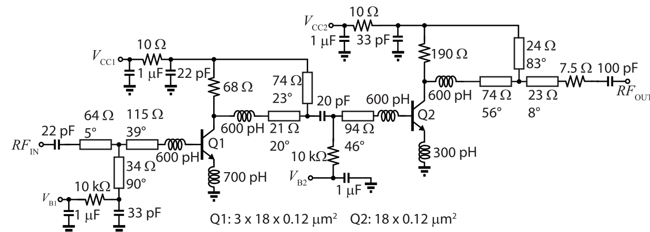

Fig. 13. Schematic diagram of demonstration amplifier. Discrete transistors fabricated in the IBM BiCMOS8HP process were used. All inductors were realized using bond wires. The 1-μF capacitors were realized using thick-film surface mount devices, whereas all other capacitances were implemented with thin-film bond-able metal–insulator–semiconductor capacitors. Standard surface mount resistors were employed for biasing and damping purposes.

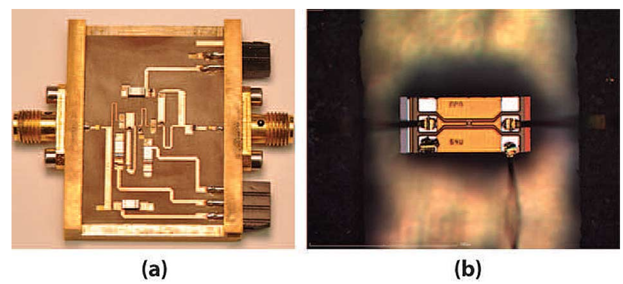

Fig. 14. Photographs of the: (a) assembled LNA module and (b) first stage transistor (Q1). The transistors were mounted in a cutout in the printed circuit board (PCB) for well-controlled wirebond lenghts. The dark regions in (b) are the PCB.

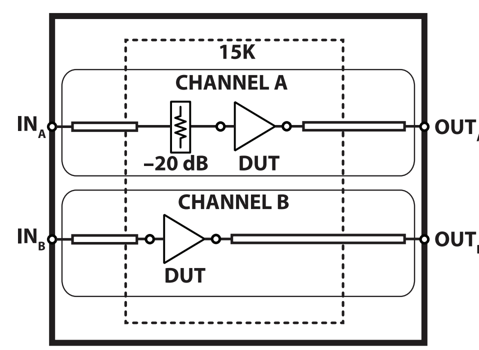

Fig. 15. Cryostat block diagram. Everything within the dashed box is heatsunk to the 15-K cold plate using indium foil and OFHC copper heat straps. Channel A was used to measure the gain and noise temperature using a noise figure analyzer. Channel B was used for scattering parameter measurements. Temperature sensors were mounted on the device-under-test (DUT) and attenuator.

forward-active mode, but is operated in saturation, will be even greater than that of $T_{\rm MIN}$ since the optimum generator impedance depends upon $V_{\rm CE}$. The magnitude of this effect depends upon the behavior of the noise resistance as a function of $V_{\rm CE}$.

$R_{\rm N}$ is plotted at 1 and 10 GHz as a function of $V_{\rm CE}$ in Fig. 11. From (9), the forward-active value of $R_{\rm N}$ is expected to be frequency independent and proportional to the physical temperature. These expectations are clearly confirmed by Fig. 11. Moreover, since the base resistance is insensitive to $V_{\rm CE}$, the noise resistance is expected to be independent of collector–emitter voltage until the device enters deep saturation. Referring to Fig. 11, this expectation is also confirmed as $R_{\rm N}$ is constant for those values of $V_{\rm CE}$ where negligible reverse currents flow. However, as the device enters deep saturation, a rapid increase in $R_{\rm N}$ was observed due to the associated drop in $I_{\rm C}$. Coupled to the rapid drop in $Z_{\rm OPT}$, this implies that the noise temperature of an amplifier designed for operation in the forward-active mode will rapidly deteriorate if operated well-into saturation. Fortunately, experimental measurements indicate that this behavior can be avoided by operating the transistors with $V_{\rm CE}$ greater than 100–200 mV, where the exact threshold depends upon the operational collector current density.

4) Associated Gain: The associated gain was also determined as a function of collector–emitter voltage and example results appear in Fig. 12. At each temperature, $G_{\rm ASSOC}$ is nearly constant for values of $V_{\rm CE}$ above approximately 200 mV. Since the observed forward-active values of $G_{\rm ASSOC}$ are well above 10 dB, these results indicate that $T_{\rm MIN} \approx T_{\rm CAS,min}$, where $T_{\rm CAS,min}$ is the minimum cascaded noise temperature as a function of generator impedance. Since the minimum cascaded noise temperature quantifies the system noise performance that is achievable by an amplifier with no passive losses, this means that it is practical to realize a high-gain cryogenic amplifier with performance approaching $T_{\rm MIN}$ [22].

As the device entered the saturation regime, a rapid decline in $G_{\rm ASSOC}$ was observed. As discussed in Section II, this effect is related to an increase in $C_{\rm CB}$ and a decrease in $f_{\rm t}$ as the device becomes saturated and is therefore more pronounced for devices operating at cryogenic temperatures.

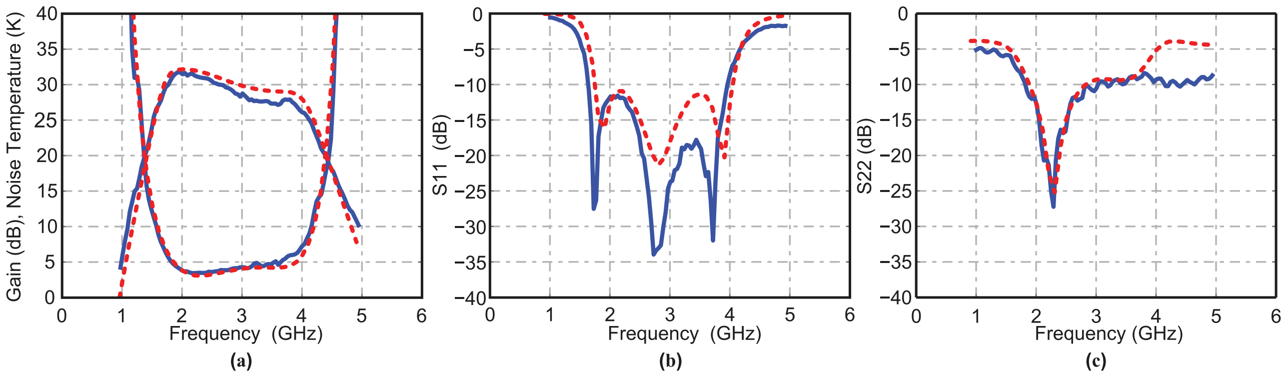

Fig. 16. Amplifier performance at 290-μW power consumption and at 15-K physical temperature. (a) Gain and noise temperature. (b) Input reflection coefficient. (c) Output reflection coefficient. The blue solid lines correspond to measurement whereas the red dashed lines correspond to model.

C. Discussion

Based upon the overall sensitivity of the noise parameters and associated gain to V_{CE}, the following broad statements can be made.

- The noise parameters and associated gain displayed little dependence upon V_{CE} provided that the device was in the forward-active region of operation. Depending upon the operational current density, the minimum collector–emitter voltage required to keep the HBT in the forward-active mode was in the range of 100–200 mV. Thus, it appears feasible to achieve optimum noise performance while operating with such values of V_{CE}.
- All of the noise parameters deteriorate in the saturation regime. That is, T_{MIN} and R_{N} increase, whereas Z_{OPT} and G_{ASSOC} shrink. This will result in a significant increase in the noise temperature of an amplifier operated in deep saturation. Thus, it is wise to set the operational point a bit above the threshold of saturation to improve robustness.

V. Proof-of-Concept Low Noise Amplifier

A two-stage 1.8–3.6-GHz amplifier was designed leveraging the small-signal noise models presented in Section IV. A schematic diagram of the amplifier appears in Fig. 13. The circuit was fabricated in a hybrid approach using discrete transistors fabricated in the IBM BiCMOS8HP technology platform. Photographs of the amplifier module and a close-up of one of the discrete transistors appear in Fig. 14.

The noise and small-signal performance of the amplifier were evaluated at 15-K physical temperature in a closed-cycle cryostat that is configured to measure the noise and small-signal performance of cryogenic amplifiers. A block diagram of the cryostat appears in Fig. 15. The gain and noise were measured using channel A of the cryostat, which is configured to support the cold attenuator method [39]. The cryogenic noise measurement system has been calibrated to a measurement accuracy that is believed to be better than ± 1 K. The reference plane for these measurements was at the coaxial terminals of the amplifier. Input and output return losses were measured using channel B of the cryostat, with the calibration referenced to the coaxial feedthroughs at the cryostat wall.

Initial measurements were made at the amplifier's nominal bias point of $V_{\mathrm{CC1}} = V_{\mathrm{CC2}} = 200$ mV, $I_{\mathrm{C1}} = 0.75$ mA, and

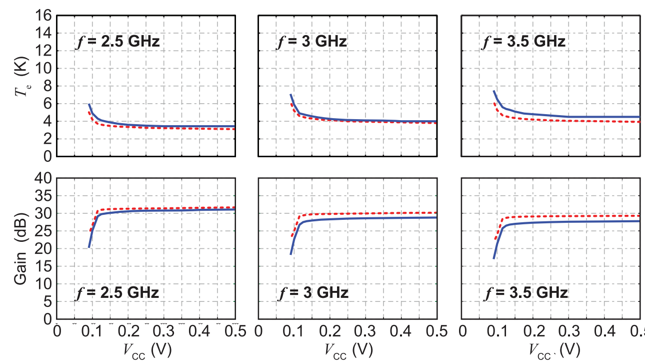

Fig. 17. Noise temperature and gain of ultra-low-power amplifier as a function of $V_{\mathrm{CC}} = V_{\mathrm{CC1}} = V_{\mathrm{CC2}}$ at 15-K physical temperature and at: (*left*) 2.5 GHz, (*center*) 3 GHz, and (*right*) 3.5 GHz. The blue solid lines correspond to measurement whereas the red dashed lines correspond to model.

$I_{\mathrm{C2}} = 0.68$ mA. The corresponding power consumption was below 290 μW. The measured gain and noise performance of the amplifier are plotted alongside the predicted performance in Fig. 16(a). The gain was greater than 27 dB and the noise temperature was between 3.4 and 5 K over the entire 1.8–3.6-GHz frequency range. These data were also found to be consistent with those predicted by simulation. The input and output reflection coefficients were measured and the results appear in Fig. 16(b) and (c). Good agreement between measurement and simulation was observed. A small discrepancy in the output return loss at higher frequencies is explained by the fact that the measurement was referred to the coaxial feedthrough at the cryostat wall and therefore included the losses of a long output cable.[3]

To confirm the results presented in Section IV, the noise and gain of the amplifier were measured as a function of $V_{\mathrm{CC1}} = V_{\mathrm{CC2}} = V_{\mathrm{CC}}$, while V_{B1} and V_{B2} were held at their nominal values. Measurement and simulation results are plotted in Fig. 17 at 2.5, 3.0, and 3.5 GHz. In each case, the gain and noise were insensitive to V_{CC} until the supply voltage reached a value of approximately 125 mV. This corner corresponds to a power dissipation of less than 180 μW and is considerably below the nominal power consumption of 290 μW. Moreover, the excellent agreement between simulation and measurement

[3]A considerably shorter input cable was employed so this effect was not as pronounced in the S_{11} measurement.

TABLE II
STATE-OF-THE-ART CRYOGENIC LNAS

	Technology -	f_{RF} (GHz)	S_{21} (dB)	T_{a} (K)	T_{e} (K)	P_{DC} (μW)
[2]	InP HEMT	4–8	40	6	2.1	4,000
[40]	InP HEMT	1–12	>37	12	4–8	15,000
[1]	InP HEMT†	4–8	44	10	1–2	4,200
[41]	InP HEMT†	4–8	>27	15	1.7	3,000
[3]	SiGe HBT	0.1–5	>30	15	4–5	20,000
[42]	SiGe HBT	0.3–5	15–18	4	8–17	2,000
[42]	SiGe HBT	0.3–8	18–25	19	6–12	8,200
[43]	SiGe HBT	0.3–4.5	>30	17	3.5–5	4,900
[44]	SiGe HBT†	0.1–0.5	>22	24	6	2,000
This work	SiGe HBT	1.8–3.6	>27	15	3.4–5	290

†*While lower power consumption were reported in these articles, the power savings came at a significant drop in performance (i.e., gain and/or noise). The numbers reported here are limited to those in which the performance was insensitive to dc power.*

offers strong support of the theoretical performance limitations discussed in Sections II and IV.

The measured performance is compared to state-of-the-art cryogenic amplifier results in Table II. In comparison to other published results, the proof-of-concept amplifier has comparable gain and noise performance. However, by operating with $V_{\mathrm{CC}} = 200$ mV, the power consumption of the amplifier is nearly an order of magnitude lower than the closest published result.[4]

VI. CONCLUSIONS

It has been shown that SiGe HBTs can operate with collector–emitter voltages in the range of 200 mV with little to no impact on the noise and small-signal performance. As a proof-of-concept, a cryogenic amplifier was demonstrated with nearly an order-of-magnitude lower power consumption compared to the state of the art. The demonstrated power savings are expected to translate to a large increase in the scalability of cryogenically cooled scientific instruments that require microwave amplifiers. For instance, the measured power consumption of just 290 μW is sufficiently low to enable a practical 1000 element dual-polarization terahertz receiver system—complete with 2000 IF amplifiers—to be cooled using a single 1.5-W capacity 4.2-K coldhead. While the bandwidth of the demonstration amplifier was limited to an octave due to the use of purely reactive tuning networks, ultra-low-power amplifiers achieving much wider bandwidths can also be realized using resistive loading and capacitively coupled feedback, albeit at a small increase in dc power consumption due to potential drops across the load resistors. Logical next steps include the development of ultra-low-power SiGe cryogenic LNAs with improved bandwidth as well as the design and implementation of integrated circuit amplifiers.

ACKNOWLEDGMENT

The authors thank S. Weinreb and E. Tong for the loan of the amplifiers used to calibrate the cryogenic measurement system and S.-W. Chang for performing the cryogenic noise calibration.

[4]It should be recognized that the frequency range of the reported amplifier is lower than that of several of the amplifiers shown in Table II. However, based on the results of Section IV, it should be feasible to achieve similar performance at frequencies up to 10 GHz while requiring little additional power.

REFERENCES

[1] J. Schleeh *et al.*, "Ultralow-power cryogenic InP HEMT with minimum noise temperature of 1 K at 6 GHz," *IEEE Electron Device Lett.*, vol. 33, no. 5, pp. 664–666, May 2012.

[2] Low Noise Factory, Göteborg, Sweden, "LNF-LNC4_8A data sheet," 2014 [Online]. Available: http://www.lownoisefactory.com/index.php/download_file/view/19/100/

[3] J. Bardin and S. Weinreb, "A 0.1-5 GHz cryogenic SiGe MMIC LNA," *IEEE Microw. Wireless Compon. Lett.*, vol. 19, no. 6, pp. 407–409, Jun. 2009.

[4] J. C. Bardin, "Silicon–germanium heterojunction bipolar transistors for extremely low-noise applications," Ph.D. dissertation, Dept. Elect. Eng., California Inst. Technol., Pasadena, CA, USA, 2009.

[5] Low Noise Factory, Göteborg, Sweden, "LNF-LNC7_10A data sheet," 2014 [Online]. Available: http://www.lownoisefactory.com/index.php/download_file/view/21/85/

[6] J. Schleeh, N. Wadefalk, P. Nilsson, J. Starski, and J. Grahn, "Cryogenic broadband ultra-low-noise MMIC LNAs for radio astronomy applications," *IEEE Trans. Microw. Theory Techn.*, vol. 61, no. 2, pp. 871–877, Feb. 2013.

[7] B. Aja Abelan *et al.*, "4–12 and 25–34 GHz cryogenic mHEMT MMIC low-noise amplifiers," *IEEE Trans. Microw. Theory Techn.*, vol. 60, no. 12, pp. 4080–4088, Dec. 2012.

[8] G. Moschetti *et al.*, "Cryogenic InAs/AlSb HEMT wideband low-noise IF amplifier for ultra-low-power applications," *IEEE Microw. Wireless Compon. Lett.*, vol. 22, no. 3, pp. 144–146, Mar. 2012.

[9] Oxford Instrum., Oxfordshire, U.K., "Triton specification sheet," Data Sheet [Online]. Available: http://www.oxford-instruments.com/OxfordInstruments/media/nanoscience/PDFs/Triton/Cryogen-Free-Helium-3-Refrigerator-Specification-Sheet.pdf, Accessed 2015.

[10] Sumitomo Cryogen., Allentown, PA, USA, "Rdk 415d capacity map," Data Sheet, 2012 [Online]. Available: http://www.shicryogenics.com/wp-content/uploads/2012/11/RDK-415D_Capacity_Map.pdf

[11] CTI Cryogen., Mansfield, MA, USA, "CTI-Cryogenics Cryodyne refrigeration system: Model 22, 350, 1020 and 1050," Data Sheet, 2002 [Online]. Available: http://www.janis.com/Libraries/10K_Coldheads/CTI-CryogenicsCryodyneRefrigerationSystemDataSheet.sflb.ashx

[12] C. Groppi *et al.*, "Supercam: A 64 pixel heterodyne array receiver for the 350 GHz atmospheric window," in *20th Int. Space Terahertz Technol. Symp.*, 2009, pp. 90–96.

[13] C. Groppi *et al.*, "The kilopixel array pathfinder project (kappa), a 16 pixel integrated heterodyne focal plane array," in *SPIE Astronomical Telescopes + Instrumentation*. Amsterdam, The Netherlands: Int. Soc. Opt. Photon., 2012, p. 84520Y.

[14] W. Shan *et al.*, "Development of superconducting spectroscopic array receiver: A multibeam 2SB SIS receiver for millimeter-wave radio astronomy," *IEEE Trans. THz Sci. Technol.*, vol. 2, no. 6, pp. 593–604, Nov. 2012.

[15] C. Walker *et al.*, "Integrated heterodyne array receivers for submillimeter astronomy," in *Astronomical Telescopes and Instrumentation*. Waikoloa, HI, USA: Int. Soc. Opt. Photon., 2003, pp. 349–354.

[16] A. Wallraff *et al.*, "Strong coupling of a single photon to a superconducting qubit using circuit quantum electrodynamics," *Nature*, vol. 431, no. 7005, pp. 162–166, Sep. 2004.

[17] C. Rigetti *et al.*, "Superconducting qubit in a waveguide cavity with a coherence time approaching 0.1 ms," *Phys. Rev. B, Condens. Matter* vol. 86, Sep. 2012 [Online]. Available: http://link.aps.org/doi/10.1103/PhysRevB.86.100506, Art. ID 100506

[18] M. Bersanelli *et al.*, "A coherent polarimeter array for the large scale polarization explorer balloon experiment," *ArXiv Preprint ArXiv:1208.0164*, 2012.

[19] M. Jung, M. Schroer, K. Petersson, and J. Petta, "Radio frequency charge sensing in InAs nanowire double quantum dots," *Appl. Phys. Lett.*, vol. 100, no. 25, 2012, Art. ID 253508.

[20] M. Shaw, J. Bueno, P. Day, C. Bradford, and P. Echternach, "Quantum capacitance detector: A pair-breaking radiation detector based on the single cooper-pair box," *Phys. Rev. B, Condens. Matter*, vol. 79, no. 14, 2009, Art. ID 144511.

[21] H. A. Haus and R. B. Adler, *Circuit Theory of Linear Noisy Networks*. New York, NY, USA: Wiley, 1959.

[22] J. Bardin and S. Weinreb, "Experimental cryogenic modeling and noise of SiGe HBTs," in *IEEE MTT-S Int. Microw. Symp. Dig.*, Jun. 2008, pp. 459–462.

[23] S. Seth, L. Najafizadeh, and J. Cressler, "On the RF properties of weakly saturated SiGe HBTs and their potential use in ultralow-voltage circuits," *IEEE Electron Device Lett.*, vol. 32, no. 1, pp. 3–5, Jan. 2011.

[24] S. Seth, C. Poh, T. Thrivikraman, R. Arora, and J. Cressler, "Using saturated SiGe HBTs to realize ultra-low voltage/power X-band low noise amplifiers," in *IEEE Bipolar/BiCMOS Circuits Technol. Meeting*, Oct. 2011, pp. 103–106.

[25] G. Niu, J. D. Cressler, S. Zhang, W. Ansley, C. S. Webster, and D. L. Harame, "A unified approach to RF and microwave noise parameter modeling in bipolar transistors," *IEEE Trans. Electron Devices*, vol. 48, no. 11, pp. 2568–2574, Nov. 2001.

[26] M. Rudolph and P. Heymann, "On compact HBT RF noise modeling," in *IEEE MTT-S Int. Microw. Symp. Dig.*, 2007, pp. 1783–1786.

[27] K. H. K. Yau, P. Chevalier, A. Chantre, and S. Voinigescu, "Characterization of the noise parameters of SiGe HBTs in the 70–170-GHz range," *IEEE Trans. Microw. Theory Techn.*, vol. 59, no. 8, pp. 1983–2000, Aug. 2011.

[28] L. Tiemeijer, R. Havens, A. B. M. Jansman, and Y. Bouttement, "Comparison of the pad-open-short and open-short-load deembedding techniques for accurate on-wafer RF characterization of high-quality passives," *IEEE Trans. Microw. Theory Techn.*, vol. 53, no. 2, pp. 723–729, Feb. 2005.

[29] J. Early, "Effects of space-charge layer widening in junction transistors," *Proc. IRE*, vol. 40, no. 11, pp. 1401–1406, Nov. 1952.

[30] E. Prinz and J. Sturm, "Analytical modeling of current gain-earth voltage products in Si/Si_{1-x} Ge_x/Si heterojunction bipolar transistors," in *Int. Electron Devices Meeting Tech. Dig.*, Dec. 1991, pp. 853–856.

[31] R. Krithivasan, Y. Lu, J. Cressler, J.-S. Rieh, M. Khater, D. Ahlgren, and G. Freeman, "Half-terahertz operation of SiGe HBTs," *IEEE Electron Device Lett.*, vol. 27, no. 7, pp. 567–569, Jul. 2006.

[32] P. Chevalier, N. Zerounian, B. Barbalat, F. Aniel, and A. Chantre, "On the use of cryogenic measurements to investigate the potential of Si/SiGe:C HBTs for terahertz operation," in *IEEE Bipolar/BiCMOS Circuits Technol. Meeting*, Sep. 2007, pp. 26–29.

[33] P. Chakraborty *et al.*, "A 0.8 THz $f_{\rm MAX}$ SiGe HBT operating at 4.3 K," *IEEE Electron Device Lett.*, vol. 35, no. 2, pp. 151–153, Feb. 2014.

[34] M. Rudolph, *Introduction to Modeling HBTs*. Norwood, MA, USA: Artech House, 2006.

[35] K. Lee, K. Choi, S.-H. Kook, D.-H. Cho, K.-W. Park, and B. Kim, "Direct parameter extraction of SiGe HBTs for the VBIC bipolar compact model," *IEEE Trans. Electron Devices*, vol. 52, no. 3, pp. 375–384, Mar. 2005.

[36] T.-R. Yang, J. M.-L. Tsai, C.-L. Ho, and R. Hu, "SiGe HBT's small-signal pi modeling," *IEEE Trans. Microw. Theory Techn.*, vol. 55, no. 7, pp. 1417–1424, Jul. 2007.

[37] Keysight Technol., Santa Rosa, CA, USA, "High-accuracy noise figure measurements using the PNA-X series network analyzer," 2014 [Online]. Available: http://literature.cdn.keysight.com/litweb/pdf/5990-5800EN.pdf?id=1961132

[38] H. Hillbrand and P. Russer, "An efficient method for computer aided noise analysis of linear amplifier networks," *IEEE Trans. Circuits Syst.*, vol. CAS-23, no. 4, pp. 235–238, Apr. 1976.

[39] J. Fernandez, "A noise-temperature measurement system using a cryogenic attenuator," *TMO Progr. Rep.*, pp. 42–135, 1998.

[40] Low Noise Factory, Göteborg, Sweden, "LNF-LNC1_12A, 1–12 GHz cryogenic low noise amplifier," Data Sheet, Aug. 2012 [Online]. Available: http://www.lownoisefactory.com/index.php/download_file/view/89/115/

[41] N. Wadefalk *et al.*, "Cryogenic wide-band ultra-low-noise IF amplifiers operating at ultra-low DC power," *IEEE Trans. Microw. Theory Techn.*, vol. 51, no. 6, pp. 1705–1711, Jun. 2003.

[42] D. Russell and S. Weinreb, "Low-power very low-noise cryogenic SiGe IF amplifiers for terahertz mixer receivers," *IEEE Trans. Microw. Theory Techn.*, vol. 60, no. 6, pp. 1641–1648, Jun. 2012.

[43] S. Weinreb, J. Bardin, H. Mani, and G. Jones, "Matched wideband low-noise amplifiers for radio astronomy," *Rev. Sci. Instrum.*, vol. 80, no. 4, pp. 044702–044702–5, Apr. 2009.

[44] H. Mani and P. Mauskopf, "A single-stage cryogenic LNA with low power consumption using a commercial SiGe HBT," in *11th Int. Low Temperature Electron. Workshop*, Jul. 2014, pp. 17–20.

Shirin Montazeri (S'14) was born in Ahvaz, Iran, on April 7, 1991. She received the B.S. degree in electrical engineering from the University of Tehran, Tehran, Iran, in 2013, and is currently working toward the Ph.D. degree in electrical engineering at the University of Massachusetts at Amherst, Amherst, MA, USA.

Since 2013, she has been a Research Assistant with the Radio Frequency Nanoelectronics Group, University of Massachusetts at Amherst. Her research interests include low-power low-noise amplifiers, RF transceivers, device modeling, and monolithic microwave integrated circuit (MMIC) design for radio astronomy applications.

Wei-Ting Wong (S'14) was born in Tainan, Taiwan, on October 3, 1982. He received the B.S. and M.S. degrees in electrical engineering from Chung Hua University, Hsinchu, Taiwan, in 2004 and 2006, respectively, and is currently working toward the Ph.D. degree at the University of Massachusetts at Amherst, Amherst, MA, USA.

From 2007 to 2011, he was a Microwave Engineer with the Academia Sinica Institute of Astronomy and Astrophysics (ASIAA). His current research interests include the design of RF integrated circuits and cryogenic low-noise amplifiers.

Ahmet H. Coskun (S'12) received the B.Sc. degree from Yeditepe University, Istanbul, Turkey, in 2011, and is currently working toward the Ph.D. degree in electrical and computer engineering at the University of Massachusetts at Amherst, Amherst, MA, USA.

His research interests include nonlinear device modeling at cryogenic temperatures and RF integrated circuit (RFIC) design for millimeter-wave applications.

Joseph C. Bardin (S'01–M'10) received the B.S. degree in electrical engineering from the University of California at Santa Barbara, Santa Barbara, CA, USA, in 2003, the M.S. degree in electrical engineering from the University of California at Los Angeles, Los Angeles, CA, USA, in 2005, and the Ph.D. degree in electrical engineering from the California Institute of Technology, Pasadena, CA, USA, in 2009.

From 2003 to 2005, he was with the Jet Propulsion Laboratory, California Institute of Technology, where he was involved in the demonstration of an array-based downlink for the NASA deep-space network. In 2010, he joined the University of Massachusetts at Amherst, Amherst, MA, USA, as an Assistant Professor with the Department of Electrical and Computer Engineering. His current research interests include reconfigurable millimeter-wave integrated circuits and built-in self test, ultra-sensitive cryogenically cooled low-noise amplifiers, transistor modeling, and novel applications of silicon integrated circuit technology for low-temperature scientific applications.

Prof. Bardin has served on the IEEE Microwave Theory and Techniques Society (IEEE MTT-S) International Microwave Symposium (IMS) Technical Program Review Committee since 2012. He was a recipient of a 2011 Defense Advanced Research Projects Agency (DARPA) Young Faculty Award, a 2014 National Science Foundation (NSF) CAREER Award, and a 2015 Office of Naval Research (ONR) YIP Award.